Open Archive TOULOUSE Archive Ouverte (OATAO)

OATAO is an open access repository that collects the work of Toulouse researchers and makes it freely available over the web where possible.

On the generation of the mean velocity profile for turbulent boundary layers with pressure gradient under equilibrium conditions

A. Rona   **M. Monti**

ar45@le.ac.uk
Department of Engineering, University of Leicester
Leicester, UK

C. Airiau

Institut de Mécanique des Fluides de Toulouse, Université de Toulouse
Toulouse, France

ABSTRACT

The generation of a fully turbulent boundary layer profile is investigated using analytical and numerical methods over the Reynolds number range $422 \leq \mathrm{Re}_\theta \leq 31{,}000$. The numerical method uses a new mixing length blending function. The predictions are validated against reference wind tunnel measurements under zero streamwise pressure gradient. The methods are then tested for low and moderate adverse pressure gradients. Comparison against experiment and DNS data show a good predictive ability under zero pressure gradient and moderate adverse pressure gradient, with both methods providing a complete velocity profile through the viscous sub-layer down to the wall. These methods are useful computational fluid dynamic tools for generating an equilibrium thick turbulent boundary layer at the computational domain inflow.

NOMENCLATURE

a	Musker profile integration constant
A	integration constant for the outer region velocity profile
B	logarithmic law constant

C_2	non-dimensional momentum thickness
C_f	wall shear stress coefficient
c_ℓ	normalised mixing length as $y \rightarrow \delta$
D_v	defect law constant in the limit $\eta \rightarrow \delta$
$\widetilde{F}$	Van Driest near-wall damping correction
F'	normalised defect velocity, $u_e^+ - u^+$
H	shape factor
i	ith data point in a discretised velocity profile
ℓ	mixing length
M	Mach number
n	mixing length blending function parameter
N	number of data points in the experimental velocity profile
p	pressure
$\Re$	real number
Re	Reynolds number
u	tangential velocity
u_τ	friction velocity
v	wall-normal velocity
x	tangential distance from the boundary layer leading edge
y	wall-normal distance from the solid wall
α	outer region normalised displacement thickness
α_m	Musker profile constant, $2\alpha_m = a - 1/\kappa$
β	normalised streamwise pressure gradient
β_m	Musker profile constant, $\beta_m^2 = 2a\alpha_m - \alpha_m^2$
$\widetilde{\beta}$	non-dimensional free-stream acceleration parameter, $\widetilde{\beta} = 2\beta F_1$
β_c	Clauser parameter
δ	boundary layer thickness
δ^*	boundary layer displacement thickness
ε	error estimate
η	outer layer non-dimensional co-ordinate, $\eta = y/\delta$
θ	boundary layer momentum thickness
κ	von Kármán constant
μ	laminar or molecular viscosity
ν	kinematic viscosity
Π	wake parameter
ρ	density
τ	tangential shear stress
τ_l	viscous shear stress
ξ	non-dimensional wall-normal distance, $\xi = y/\delta$

Subscripts

a	analytical prediction
e	free-stream condition
l	viscous length scale
n	result numerically obtained
r	reference value, from experiment or direct numerical simulation

t	Reynolds average (turbulent) component
w	wall condition
0	leading edge condition
1	boundary layer edge condition, $\eta = 1$

Superscripts

+	inner layer scaling
$\overline{(\ )}$	time average
'	fluctuation about the time-mean value

1.0 INTRODUCTION

Computational fluid dynamic (CFD) simulations of wall-bounded flows, such as the flow over aircraft high-lift devices, ailerons, the elevators and the rudder, often use a turbulent boundary layer inflow to reduce the computational domain size with respect to a full wing, tailplane or fin simulation. The quality of the numerical predictions can be significantly affected by how well the boundary layer inflow is modelled. For instance, in a cavity, the inflow momentum thickness has a direct influence on the acoustic mode selection[1]. This paper compares the use of analytical correlations and of an auxiliary boundary layer numerical method for generating a turbulent boundary layer inflow for CFD over a wide Reynolds number range.

Where the inflow features a fully developed turbulent boundary layer, an analytical profile for the mean velocity can be imposed, derived from the integral boundary layer parameters as determined from either a larger-scale numerical simulation or from experiment. In a non-dimensional simulation, the inflow may be specified based on the inflow Mach number M, boundary layer thickness-based Reynolds number Re_τ, shape factor H, and the Clauser parameter β_c for the streamwise pressure gradient.

Analytical semi-empirical approaches for specifying a fully turbulent incompressible boundary layer under equilibrium conditions have received significant attention in the literature, starting from the scaling arguments of Millikan[2], the logarithmic overlap of von Kármán[3], the composite profile of Coles[4], and more recent analytical profiles by Chauhan *et al*[5]. The predictive ability of the more widely used analytical profiles are reviewed by Panton[6] and Buschmann and Gad-el-Hak[7].

This work uses the composite law of the wall approach of Coles[4], adding to this class of formulations that is reviewed by Lewkowicz[8], Sandham[9], Örlü *et al*[10], and Rona and Grottadaurea[11]. The predictive ability of the composite law of the wall presented in this paper, which uses the defect law of Finley *et al*[12], is tested by defining a diagnostic function, following Zagarola and Smits[13], that is analogous to the FD function used in the comparative analysis among analytical velocity profiles in Buschmann and Gad-el-Hak[7].

An alternative approach to defining the mean velocity inflow is the use of an auxiliary numerical simulation of the upstream boundary layer obtained, for instance, from running two-dimensional companion software by Wilcox[14]. This work uses a numerical method derived from the theory of the interactive boundary layer of Cousteix and Mauss[15,16].

The interactive boundary layer (IBL) model of Cousteix and Mauss[15,16] consists in a uniformly valid approximation of the velocity field, including the inner and the outer regions, of an incompressible turbulent boundary layer. It provides rational mathematical arguments in the form of a method of matched asymptotic expansions (MAE). The model is obtained by successive complementary expansions of the velocity profiles in the inner and in the outer regions of the

boundary layer. It is equivalent to the method of matched asymptotic expansions associated to the Van Dyke matching principle. This approach enables to achieve engineering accurate solutions of the boundary layer flow in regions of different scaling with strong non-linear interaction. The interactive boundary layer method departs from previous composite formulations for the mean velocity profile in that it does not necessitate any overlap in the logarithmic region. The flow governing equations are solved simultaneously and the only requirement for modelling a turbulent boundary layer is to couple the matched asymptotic expansions to a mixing length model that is compatible with the log law. This is an advantage over other formulations. A second advantage of the interactive boundary layer model is that the matching in the expansion is stated about a parameter that is required to be small but finite, as opposed to infinitely small. This avoids an important source of numerical underflow in its implementation on a computer platform.

This work introduces a novel element in the interactive boundary layer model of Cousteix and Mauss[15,16]. Specifically, Section 3.2 introduces a new blending function in the mixing length model used in this numerical method. The new function features an adjustable parameter n that is shown in Section 4.4 to give an improved mixing length profile across the boundary layer compared to the blending function of Michel *et al*[17] and to the mixing length model by Spalding[18] reported in Galbraith and Head[19]. The analytical and numerical approaches are then applied to model a boundary layer with and without an adverse streamwise pressure gradient. The remainder of the paper is structured in five sections. Section 2 presents the benchmark velocity profiles that are used in Sections 4 and 5 for the validation of the analytical and numerical predictions. Section 3.1 details the analytical method used to generate the composite velocity profile in a turbulent boundary layer. Section 3.2 details the numerical method based on the interactive boundary layer model. Section 4 validates both methods using zero pressure gradient velocity data over the Reynolds number range $422 \leq \mathrm{Re}_\theta \leq 31{,}000$ and presents a comparison of the new mixing length model with other mixing length schemes and experiment. Section 5 extends the validation to adverse pressure gradient boundary layers and summarises the limitations of the numerical methods. Concluding remarks are given in Section 6.

2.0 REFERENCE VELOCITY PROFILES

This section presents a selection of the experimental and direct numerical simulation data on turbulent boundary layers available in the open literature. This data is used to benchmark the analytical and numerical methods for generating turbulent boundary layer inflow profiles in Sections 4 and 5. The selected data span over ten years, are test facility non-specific, and are obtained by direct numerical simulation (DNS) and hot-wire (HW) anemometry. From the documentation accompanying each data set, estimates of the uncertainty in the mean velocity profile are obtained, so that this can be used in the assessment of the predicted mean velocity in Sections 4 and 5. In the wind tunnel tests, the quality of the turbulent boundary layer benchmark data depends on the facility as well as on the measurement technique. Two main influential factors are the measurement accuracy of the wall-normal distance, as highlighted in Örlü *et al*[10], and that of the wall friction velocity u_τ, which is used in the scaling laws of Section 3. Velocity measurements in which efforts were made towards quantifying and reducing the uncertainty from both factors were obtained by the International Collaboration on Experiments in Turbulence (ICET) consortium. These measurements used oil film interferometry (OFI) to obtain an independent estimate of the local wall shear stress coefficient τ_w from which u_τ is derived. Österlund[20] reports velocity measurements obtained using the OFI technique in which estimates of the uncertainty in u_τ and in the wall-normal distance are given. These are used as the main reference velocity profiles in this paper. These

Reference	Re_θ	Re_r	u_e^+	u_r method	u method	Symbol
Skote[21]	422	222	19·54		DNS	▽
Skote[21]	588	272	20·45		DNS	✿
Skote[21,22]	606	251	20·60		DNS	▽
Skote[21,22]	681	251	21·70		DNS	○
Erm and Joubert[23]	697	335	20·25	Preston tube	Pitot	*
Erm and Joubert[23]	1,003	460	21·5	Preston tube	Pitot	Δ
De Graaff and Eaton[24]	1,430	640	22·4	Fit to Equation (3)	LDA	•
De Graaff and Eaton[24]	2,900	1,192	24·33	Fit to Equation (3)	LDA	◀
Österlund[20]	3,654	1,365	25·38	OFI	HW	×
De Graaff and Eaton[20]	5,200	2,000	26	Fit to Equation (3)	LDA	▶
Österlund[20]	12,633	4,436	28·62	OFI	HW	□
De Graaff and Eaton[24]	13,000	4,770	28	Fit to Equation (3)	LDA	◇
Österlund[20]	22,845	8,000	30·15	OFI	HW	★
De Graaff and Eaton[24]	31,000	13,030	30	Fit to Equation (3)	LDA	+

Table 2
Uncertainty estimate in the reference velocity profiles

Reference	Profile no.	Re_θ	$\varepsilon(y^+)$ (%)	$\varepsilon(\tau_w)$ (%)	$\varepsilon(u^+)$ (%)
Skote[21]	ZPG u200	422	0·04		2·5
Skote[21]	ZPG u350	588	0·04		2·5
Skote[21,22]	APG1 u350	606	0·05		2·5
Skote[21,22]	APG2 u335	681	0·03		2·5
Erm and Joubert[23]		697	12·18		
Erm and Joubert[23]		1,003	11·91		
De Graaff and Eaton[24]		1,430	0·30		1·5
De Graaff and Eaton[24]		2,900	0·46		1·5
Österlund[20]	SW981128A	3,654	0·14	4	0·5
De Graaff and Eaton[24]		5,200	0·83		1·5
Österlund[20]	SW981005A	12,633	0·25	4	0·5
De Graaff and Eaton[24]		13,000	2·15		1·5
Österlund[20]	SW981006B	22,845	0·48	4	0·5
De Graaff and Eaton[24]		31,000	4·94		1·5

uncertainty estimates enable to judge to what extent the differences among the predicted profiles and the benchmark ones presented in Sections 4 and 5 are significant.

Table 1 lists the sources of reference velocity profiles with the main non-dimensional parameters as reported by each author. Table 2 presents an estimate of the uncertainty associated with the reference data, due to the velocity, wall shear stress, and vertical displacement measurement techniques used in each case. These are combined under the assumption of statistical independence to obtain a first estimate of the uncertainty in the non-dimensional reference velocity u_r^+ near the wall. The uncertainty in u_r^+ from Skote[21] is based on the difference between predicted profiles in the computational mesh convergence study of Skote *et al*[22]. Where authors have identified their profiles with a labelling system, such as a serial number, this is reported in Table 2 for clarity. In Skote[21], the wall-normal spatial position accuracy is estimated as one DNS mesh height from the wall. In Erm and Joubert[23], this is estimated as half the pitot probe height. In De Graaf and Eaton[24], the laser doppler anemometry (LDA) half beam height is used. In Österlund[20], the uncertainty from using a telescopic height finder is given by the author. These uncertainties are stated in Table 2 in wall units, normalised

by the values for u_τ and kinematic viscosity ν listed by each author. This uncertainty analysis gives some appreciation of the advances in measurement techniques and efforts made to provide quality benchmark velocity profiles with clearly defined uncertainty margins in support of the on-going boundary layer modelling research.

Erm and Joubert[23] explore the effect of the tripping device on the characteristics of the generated turbulent boundary layer in flat plate wind tunnel experiments. They show that the appropriateness of tripping devices is velocity-dependent, with the correct stimulation being such that it just enables the boundary layer to become turbulent. This is verified by surveying the kinetic energy spectrum downstream of the tripping devices, which displays a uniform energy cascade when this condition is met. Practical solutions for obtaining such a condition at low Reynolds numbers are presented and tested in Rona and Soueid[25]. Whereas a monotonic kinetic energy cascade in the kinetic energy spectrum is only one marker of a fully developed turbulent boundary layer, the reference velocity profiles in Table 1 have been selected based on the availability of kinetic energy spectra that document such a feature.

3.0 ANALYTICAL AND NUMERICAL METHODS

3.1 Analytical method

To describe the mean velocity profile in a turbulent boundary layer, similarity solutions are sought in the inner and in the outer regions. In the inner region, the mean streamwise velocity u scales with the wall friction velocity u_τ and with the viscous length scale $l = \nu/u_\tau$, so that

$$\frac{u}{u_\tau} = f\left(y^+\right) \qquad \qquad \ldots (1)$$

where $y^+ = y\, u_\tau\, /\nu$ is the inner scaling non-dimensional wall-normal distance. In the outer region, the velocity profile is described by the velocity defect law

$$\frac{u_e - u}{u_\tau} = F'\left(\eta\right) \qquad \qquad \ldots (2)$$

where $\eta = y/\delta$ is the outer scaling non-dimensional wall-normal distance, u_e is the free-stream velocity, ν is the kinematic viscosity, y is the wall-normal distance, and δ is the boundary layer thickness, which is taken as the wall-normal distance at which $u = 0{\cdot}95u_e$.

Millikan[2] suggested that, at a sufficiently high boundary-layer Reynolds number $Re_\tau = u_\tau\delta/\nu$, an overlap between the inner and the outer regions is present, in which both scaling laws hold. Matching the velocity profile gradients from Equations (1) and (2) gives in this overlap region a constant logarithmic gradient, as previously obtained by von Kármán[3] by dimensional analysis. This asymptote is expressed by the von Kármán law of the wall

$$u^+ = \frac{1}{\kappa}\ln y^+ + B \qquad \qquad \ldots (3)$$

where $u^+ = u/u_\tau$ is the normalised streamwise velocity, κ is the von Kármán constant, and B is the logarithmic law constant.

In the inner region, the velocity profile close to the wall at $1 \leq y^+ \leq 4\cdot7$ is driven by viscosity, resulting in a viscous sub-layer where $u^+ = y^+$. Analytical solutions that blend the near-wall linear mean velocity profile with the logarithmic law of Equation (3) are given by Rotta[26], Reichardt[27], van Driest[28], Spalding[29], Musker[30], Nitsche et al[31], and Chauhan et al[5]. These are reviewed in Örlü et al[10]. The profile by Spalding[29] is a power-series interpolation scheme[32] in the form

$$ y^+ = u_i^+ + \exp(-\kappa B)\left[\exp\left(\kappa u_i^+\right) - 1 - \frac{\left(\kappa u_i^+\right)^2}{2} - \frac{\left(\kappa u_i^+\right)^3}{6} \right] \qquad \ldots (4) $$

where subscript i denotes the inner region. The profile by Musker[30] is a profile of velocity gradient with an integral solution by partial fractions given in Monkewitz et al[33] as

$$ u_i^+ = \frac{1}{\kappa}\ln\left(\frac{y^+ + a}{a}\right) + \frac{\alpha_m}{a + 4\alpha_m}\left\{ (a - 4\alpha_m)\ln\left[\frac{a\left[\left(y^+ - \alpha_m\right)^2 + \beta_m^2\right]}{2\alpha_m\left(y^+ + a\right)^2}\right] \right. $$
$$ \left. + \frac{2\alpha_m(5a - 4\alpha_m)}{\beta_m}\left[\arctan\left(\frac{y^+ - \alpha_m}{\beta_m}\right) + \arctan\left(\frac{\alpha_m}{\beta_m}\right)\right]\right\} \qquad \ldots (5) $$

where $2\alpha_m = a - 1/\kappa$, $\beta_m^2 = 2a\alpha_m - \alpha_m^2$, and $a = 10\cdot306$.

The logarithmic overlap between the inner and the outer regions allows combining Equations (1) and (2) by addition, as in Coles[4], in which the outer region velocity profile is expressed in terms of the inner scaling variables by the addition of a wake function:

$$ u^+ = u_i^+ + \frac{\Pi}{\kappa} f(\eta) $$

where Π is the wake parameter and $\eta = y^+/\mathrm{Re}_\tau$. Analytical expressions for the wake function f (η) are given by Coles[4], Moses[34], Finley et al[12], and Chauhan et al[5]. These formulations are reviewed in Lewkowicz[8], Sandham[9], Örlü et al[10], and Rona & Grottadaurea[11]. Adding the wake function of Finley et al[12] to Equation (4) and (5) gives a single analytical explicit expression for the velocity distribution across a turbulent boundary layer

$$ u^+ = \underbrace{u_i^+ + \frac{1}{\kappa}\eta^2(1 - \eta)}_{\text{Pure wall flow}} + \underbrace{2\frac{\Pi}{\kappa}\eta^2(3 - 2\eta)}_{\text{Pure wake component}} \qquad \ldots (6) $$

The wake parameter Π represents the departure of the velocity profile from Equation (3) at $y^+ = \mathrm{Re}_\tau$. From Coles[4], imposing $u^+ = u_e^+$ at $y^+ = \mathrm{Re}_\tau$ in Equation (6), with u_i^+ from Equation (3), gives

$$ \Pi = (\kappa/2)\left(u_e^+ - \kappa^{-1}\ln\mathrm{Re}_\tau - B\right) \qquad \ldots (7) $$

where $u_e^+ = u_e/u_\tau$ is the normalised free-stream velocity.

The composite velocity profile of Equation (6) is a linear expression that can be evaluated analytically. In combination with Equation (5), the profile is explicit in y^+ and satisfies the boundary conditions

$$u\big|_{y=\delta} = u_e \qquad \qquad \ldots (8)$$

and

$$\frac{\partial u}{\partial y}\bigg|_{y=\delta} = 0 \qquad \qquad \ldots (9)$$

Equation (6) is similar to the law of the wall and law of the wake by Moses[34]. In addition, it allows a conformal mapping to recover the Coles' form of the law of the wake, as shown by Rona & Grottadaurea[11]. Equation 6 is tested against experimental velocity profiles over a relatively wide range of momentum thickness-based Reynolds numbers $Re_\theta = u_e\theta/\nu$ in Section 4. To evaluate Equation (6), the authors take $\kappa = 0.384$ and $B = 4.17$, which were shown in Monkewitz *et al*[33] to fit the experimental velocity profiles from Österlund[20].

The quality of the fit to individual experimental profiles can be improved by treating κ and B as closure constants. These can be determined by a bivariate regression, as in Krogstad *et al*[35]. Regressed κ and B values for the outer layer experimental profiles used in Section 4.1 are given in Rona and Grottadaurea[11]. As one aim of this paper is to introduce methods for generating an inflow velocity profile for RANS computations, rather than curve-fitting specific traverses, the authors take $\kappa = 0.384$ and $B = 4.17$ constant. These are average values from 385 mean velocity profiles, from Monkewitz *et al*[33].

3.2 Interactive boundary layer method

The method for obtaining an interactive boundary layer model is detailed in Cousteix and Mauss[15] and this paper only reproduces the key steps that support the authors' application to turbulent boundary layers.

Across the boundary layer, the local shear stress

$$\tau = \mu\frac{\partial u}{\partial y} - \rho\overline{u'v'} = \mu\frac{\partial u}{\partial y} + \tau_t \qquad \qquad \ldots (10)$$

where u' and v' are the time-dependent fluctuations of the streamwise and flow-normal velocity components and are unknowns. To avoid having to resolve these unknowns, the Reynolds shear stress τ_t is evaluated using Prandtl's mixing length model[36], with the Van Driest[37] near-wall damping correction $\widetilde{F}$. This gives

$$\tau_t = \rho\widetilde{F}^2\ell^2\left|\frac{\partial u}{\partial y}\right|\left(\frac{\partial u}{\partial y}\right) \qquad \qquad \ldots (11)$$

where $\widetilde{F} = 1 - \exp(-y^+/26)$.

In the inner region, $\ell = \kappa y$, while in the outer region, $\ell/\delta \to c_\ell$ as $y \to \delta$ and $c_\ell = 0.085$. These two trends can be merged analytically into a single distribution for the mixing length ℓ across the full boundary layer by the use of a blending function. Michel *et al*[17] use the blending function

$$\ell(\eta) = \delta c_\ell \tanh\left(\frac{\kappa\eta}{c_\ell}\right) \qquad \qquad \ldots (12)$$

with $\kappa = 0.41$. The authors propose an alternative blending function that is shown in Section 4 to give an improved prediction of the normalised eddy viscosity profile at the interface between the inner and the outer layer, at a Reynolds number Re_τ of 1,000. This is

$$\ell(\eta) = \delta \frac{\kappa\eta}{\left[1+\left(\kappa\eta/c_\ell\right)^n\right]^{1/n}} \qquad \dots (13)$$

For $2.6 < n < 2.7$, the $\ell(\eta)$ profile from Equation (13) almost matches that from Equation (12).

3.3 The defect law and the viscous sub-layer

3.3.1 Inner region velocity profile

Normalising the local shear stress τ in Equation (11) by ρu_τ^2 and assuming a monotonic velocity profile gives

$$\frac{\tau}{\tau_w} = \frac{\partial u^+}{\partial y^+} + \ell^{+2}\widetilde{F}^2\left(\frac{\partial u^+}{\partial y^+}\right)^2 \qquad \dots (14)$$

where $\ell^+ = \ell u_\tau/\nu$. In the limit $y^+ \to 0$, $\tau \to \tau_w$ and Equation (14) becomes

$$1 = \frac{\partial u^+}{\partial y^+} + \ell^{+2}\widetilde{F}^2\left(\frac{\partial u^+}{\partial y^+}\right)^2 \qquad \dots (15)$$

Equation (15) is a quadratic in $\partial u^+/\partial y^+$ with root[15]

$$\frac{\partial u^+}{\partial y^+} = \frac{2}{1+\sqrt{1+4\left[\ell^+\left(y^+\right)\widetilde{F}\left(y^+\right)\right]^2}} \qquad \dots (16)$$

Integrating Equation (16) with respect to y^+ with the boundary condition $u^+(x,0) = 0$ gives the inner layer tangential velocity profile that asymptotes to the von Kármán law of the wall of Equation (3) for $y^+ > 80$ with $B = 5.28$.

3.3.2 Outer region velocity profile

In an equilibrium turbulent boundary layer, a similarity solution for the outer layer is sought in terms of the velocity defect $F'(\eta) = u_e^+ - u^+$, under the local assumption of no boundary layer growth. Expressing τ/τ_w as a function of F and η gives[15]

$$\tau^+ = \frac{\tau}{\tau_w} = 1 - \frac{F}{F_1} + \left(\frac{1}{F_1}+2\beta\right)\eta F' \qquad \dots (17)$$

where

$$F = \int_0^\eta F'(\xi)\,\mathrm{d}\xi; \quad F_1 = F(1); \quad \beta = -\frac{\delta}{u_\tau}\frac{\mathrm{d}u_e}{\mathrm{d}x} \qquad \dots (18)$$

from which $u_e\delta^*/\nu = F_1 Re_\tau$, where δ^* is the boundary layer displacement thickness.

In the outer region, the Reynolds stress component is dominant over the non-turbulent shear stress, so $\tau \approx \tau_t$. From Equation (11), noting that the Van Driest damping function $\tilde{F} \to 1$ for $y^+ \geq 100$, $\tau/\tau_t = (\ell/\delta)^2\, F''^2$, where $F'' = dF'/d\eta$. Substituting $(\ell/\delta)^2\, F''^2$ for τ/τ_w in Equation (17), the similarity solution for the outer region becomes

$$\left(\frac{\ell}{\delta}\right)^2 F''^2 = 1 - \frac{F}{F_1} + \left(\frac{1}{F_1} + 2\beta\right)\eta F' \qquad \ldots (19)$$

3.3.3 Wall shear stress coefficient

A matching condition is sought for the velocity profiles of the inner and outer regions, Equations (16) and (19). This is obtained from standard asymptotic analysis[15] by considering Equation (16) in the limit $y^+ \to \infty$ and Equation 19 in the limit $\eta \to 0$ that give respectively[15]

$$u^+ = \kappa^{-1} \ln y^+ + B \qquad \ldots (20)$$

$$u_e^+ - u^+ = -\kappa^{-1} \ln \eta + D_v \qquad \ldots (21)$$

Adding Equation (20) to Equation (21) gives[15]

$$u_e^+ = \kappa^{-1} \ln \frac{u_\tau \delta}{\nu} + B + D_v \qquad \ldots (22)$$

Equation 22 can be re-cast as function of the wall shear stress coefficient $C_f = \tau_w /(0\ 5\rho u_e^2)$ that is imposed as equal in the inner and outer regions and provides the matching criterion for the two profiles at Re_τ

$$\sqrt{\frac{2}{C_f}} = \kappa^{-1} \ln \mathrm{Re}_\tau + B + D_v \qquad \ldots (23)$$

3.4 Numerical implementation

Determining the outer region velocity profile from the numerical solution of Equation (19) poses several challenges. Equation 19 is non-linear and is ill-defined at the upper boundary layer limit, as $\eta \to 1$, where $F'' \to 0$, and at the lower boundary layer limit, as $\eta \to 1$, where $\ell/\delta \to 0$ and $F'' \to \infty$. To solve this limit value problem, auxiliary approximate solutions are imposed on the floor of the viscous sub-layer and at the edge of the boundary layer, as shown in Fig. 1, so that the edges of the inner and of the outer regions are modelled analytically while the overlap region is resolved numerically.

Let $f(\eta) = F(\eta)/F(1)$. On the floor of the viscous sub-layer, imposing $\eta = 0$ and $\ell = \kappa y$, as in Section 3.2, Equation (19) becomes

$$\left[\kappa\eta F_1 f''(\eta)\right]^2 = 1 - f(\eta) + (1 + 2\beta F_1)\eta f'(\eta) \qquad \ldots (24)$$
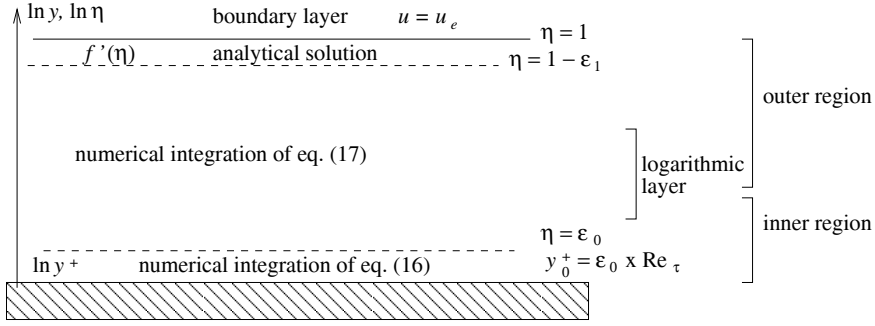
with the boundary condition $f(0) = 0$. Let

Figure 1. Boundary layer decks.

$$\tilde{\beta} = 2\beta F_1 \qquad \qquad \cdots (25)$$

$\tilde{\beta}$ allows to model the presence of a non-zero streamwise pressure gradient if $\beta \neq 0$. In a zero pressure gradient boundary layer, $\beta = 0$ by Equation (18), for which Equation (24) has the explicit solution

$$f(\eta) = \frac{\eta^2}{4\alpha^2} - \frac{\eta \ln \eta}{\alpha} + A\eta; \, f'(\eta) = \frac{\eta}{2\alpha^2} - \frac{1 + \ln \eta}{\alpha} + A; \, f''(\eta) = \frac{1}{2\alpha^2} - \frac{1}{\alpha \eta}$$

with $\alpha = F_1 \kappa$. The integration constant A is determined by evaluating $f'(\eta)$ at $\eta = \varepsilon_0$ on the floor of the viscous sub-layer. In a non-zero pressure gradient boundary layer, $\tilde{\beta} \eta f' \to 0$ as $\eta \to 0$. The term β has a weak influence approaching the wall, hence the zero pressure gradient profile is used on the floor of the viscous sub-layer for all β.

At the edge of the boundary layer, at $\eta = 1$, Equation (19) becomes

$$\left[\ell_1 F_1 f''(\eta) \right]^2 = 1 - f(\eta) + \left(1 + \tilde{\beta} \right) \eta f'(\eta) \qquad \cdots (26)$$

with the boundary conditions $f(1) = 1$, $f'(1) = 0$, $f''(1) = 0$ and ℓ_1 evaluated from Equation (13) at $\eta = 1$. Cousteix[38] proposed the solution for Equation (26)

$$f(\eta) = 1 - \frac{(1 - \eta)^3}{3}; \, f'(\eta) = (1 - \eta)^2; \, f''(\eta) = -2 + 2\eta \qquad \cdots (27)$$

for $\beta = 0$, which has the attractive property of being independent from F and ℓ_1 and is the solution used in this work. The same solution is used for $\beta \neq 0$, as $\tilde{\beta} \eta f'(1) = 0$ by the boundary condition $f'(1) = 0$ in Equation (26).

An additional difficulty is introduced for $\beta \neq 0$. The term βF_1 is in fact unknown *a priori* since F_1 can be evaluated from the solution of the problem only if β is initially fixed. As F_1 is a problem output, Equation (25) can be solved using a standard Newton-Raphson method. Let $\tilde{\beta}_i$ be the i-th estimate of $\tilde{\beta}$ in the Newton-Raphson procedure. This is related to the pressure gradient β by

$$\beta(\tilde{\beta}_i + \Delta\tilde{\beta}_i) = \beta(\tilde{\beta}_i) + \frac{d\beta}{d\tilde{\beta}} \Delta\tilde{\beta}_i = \beta_{\text{target}} \qquad \cdots (28)$$

from which the correction $\Delta\tilde{\beta}_i = 2F_1(\beta_{\text{target}} - \beta(\tilde{\beta}_i))$ is obtained and $\tilde{\beta}_{i+1} = \tilde{\beta}_i + \Delta\tilde{\beta}_i$, iterating until convergence.

Table 3
Analytical and numerical velocity profiles. $n = 4$ **in Equation (13)**

Reference	Re_θ	Π	$(Re_\tau)_n$	$(u_e^+)_n$
Skote[21]	422	0·298	220	19·8
Skote[21]	588	0·385	270	20·5
Erm and Joubert[23]	697	0·219	315	20·77
Erm and Joubert[23]	1,003	0·317	446	21·66
De Graaff and Eaton[24]	1,430	0·336	627	22·51
De Graaff and Eaton[24]	2,900	0·421	1,240	24·17
Österlund[20]	3,654	0·568	1,551	24·71
De Graaff and Eaton[24]	5,200	0·505	2,185	25·54
Österlund[20]	12,633	0·643	5,188	27·65
De Graaff and Eaton[24]	13,000	0·480	5,335	27·72
Österlund[20]	22,845	0·662	9,258	29·06
De Graaff and Eaton[24]	31,000	0·388	12,845	29·79

4.0 THE ZERO PRESSURE GRADIENT BOUNDARY LAYER

4.1 Overview of the results

The analytical and numerical methods for predicting a turbulent boundary layer mean velocity profile of Section 3 are tested against a range of streamwise velocity measurements and direct numerical simulations of zero pressure gradient boundary layers[20-24] over the range $422 \leq Re_\theta \leq 31,000$. The analytical profiles use the values of u_e^+ and Re_τ in the reference data, listed in Table 1, while Π is determined from Equation (7) and is reported in Table 3. Alternatively, Π can be obtained by fitting Equation (6) using a least squares regression approach, as in Rona and Grottadaurea[11], which decreases the sensitivity of the fitted profile on the definition of Re_τ in the reference data. In the interactive boundary layer method of Section 3.2, Re_τ and u_e^+ are implicit variables that are obtained by iteration. In Table 3, $(Re_\tau)_n$ and $(u_e^+)_n$ are the results from the converged iterations of the numerical method for each reference profile.

4.2 Analytical, experimental, and direct numerical simulation velocity profiles

The normalised mean streamwise velocity u^+ is plotted against the normalised wall-normal distance y^+ in Fig. 2 for different Reynolds numbers. The symbols used in Fig. 2 are the benchmark data[20-24] at different Re_θ from Section 2, labelled as in Table 1. The continuous lines show the fitted analytical profiles from Equations (5) and (6). For clarity, an incremental shift of $u^+ = 2·5$ is applied to all curves, with the origin on the vertical axis referring to the $Re_\theta = 422$ velocity profile.

The reference profiles in Fig. 2 are ordered in ascending Re_θ. The profiles from DNS at $Re_\theta = 422$ and $Re_\theta = 588$ are below the remainder profiles from experiment. The fitted analytical curves for $Re_\theta = 422$ (dashes) and $Re_\theta = 588$ (dash-dots) are shown in Fig. 2 together with the experimental profiles to assess the quality of the analytical fit to the DNS data as compared to the experimental data. The analytical profiles display an appreciable fit to the reference data over the range $422 \leq Re_\theta \leq 31,000$. The experimental data seem to be randomly distributed about each fitted curve with no underlying trend, suggesting that the analytical method has captured most of the u^+ dependence on δ, u_e, u_τ, and Re_θ.
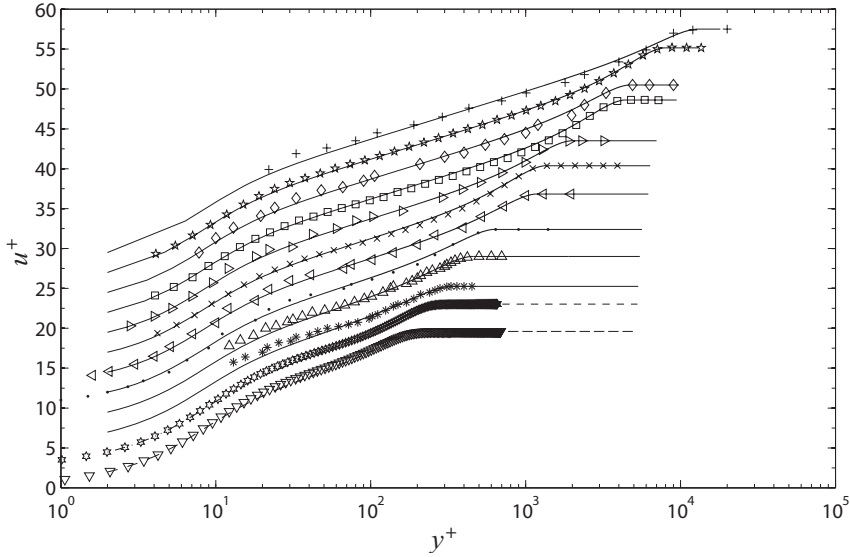
Figure 2. Turbulent boundary layer profiles from experimental
data and DNS fitted to Equation (6). Symbols as in Table 1.

Figure 3 shows the effect of using the composite velocity profile of Equation (6) in combination with Equation (4) and Equation (5). The symbols are the hot-wire measurements from Österlund[20] at Re_θ = 3,654, 12,633 and 22,845. The measurements at Re_θ = 12,633 are the same SW981005A Österlund hot-wire data used by Kendall and Koochesfahani[32] to study the fitting of Equations (4) and (5) in the inner region of the boundary layer. This study widens the benchmark data range to 3,654 ≤ Re_θ ≤ 22,845 and uses a composite velocity profile.

In Fig. 3, the continuous line is the composite velocity profile for Re_θ = 12,633 that uses the Musker[30] law of the wall for the inner layer. The dashed line is the composite velocity profile that uses the Spalding[29] law of the wall for the inner layer. The von Kármán law of the wall of Equation (3) is shown by a dash-dot line, for reference. Using the Musker[30] law of the wall in the form of Equation (5) in the composite profile of Equation (6) gives a marginally better fit to the experimental data in the region of transition between the viscous sub-layer and the logarithmic overlap region than using the Spalding[29] law of the wall in Equation (6). This agrees with the inner layer velocity profile comparison by Kendall and Koochesfahani[32], in which a composite velocity profile was not used, where the authors note a similar advantage in using the Musker[30] law of the wall over the Spalding[29] law of the wall.

Figure 4 shows the outer portion of the velocity profile at Re_θ = 12,633 using the same notation as Fig. 3. In the outer profile, the use of the Spalding[29] law of the wall in the composite profile of Equation (6) gives a marginally better fit to the SW981005A hot-wire data.

A further quantitative insight into the quality of the analytical predictions from the composite profile computed with either Equation (4) or Equation (5) is obtained by defining a diagnostic function, following the example of Zagarola and Smits[13].

The percentage difference between the analytical prediction of the streamwise velocity and the corresponding hot-wire measurement across the boundary layer is defined as the diagnostic function
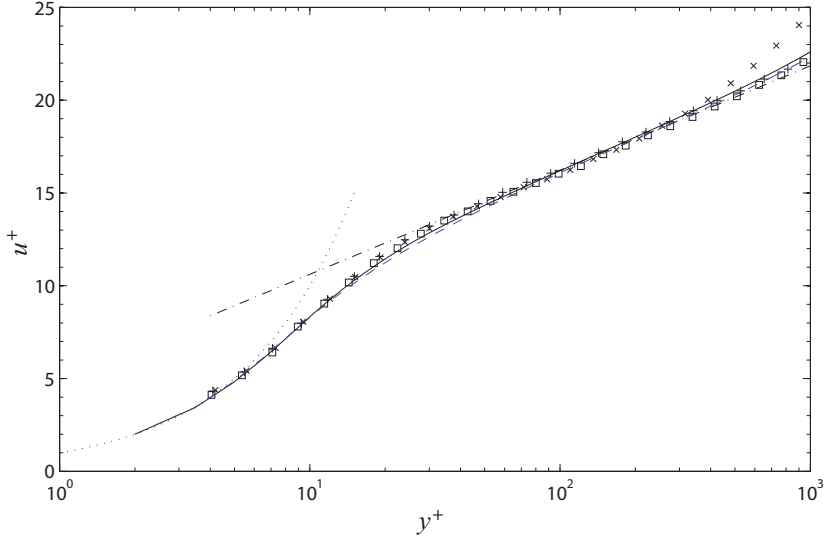
Figure 3. Inner layer velocity profiles from Österlund[20] (symbols) and from Equation 6 (lines). Inner law of the wall from (—) Musker[30], (– –) Spalding[29], and (– · –) von Kármán[3]. (···) u+ = y+. Symbols as in Table 1.
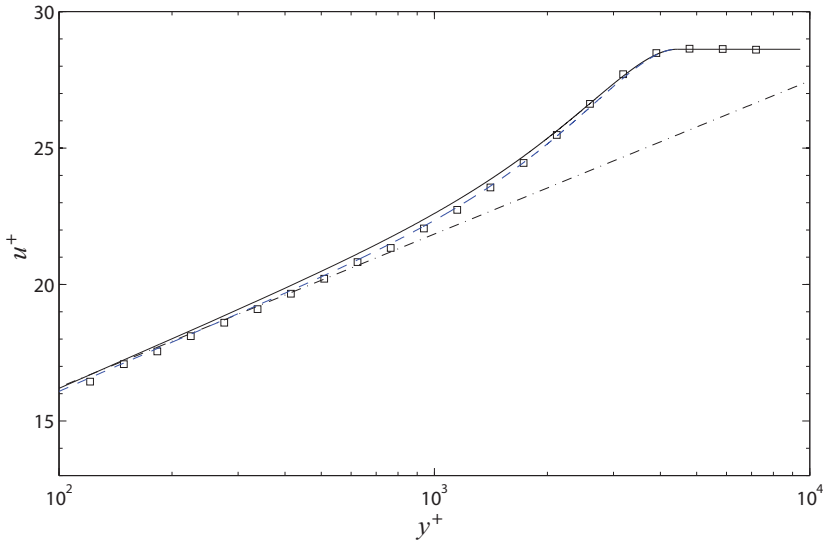

Figure 4. Outer layer velocity profiles from Österlund[20] (symbols) and from Equation (6) (lines) at. Inner law of the wall from (—) Musker[30], (– –) Spalding[29], and (– · –) von Kármán[3].

$$\varepsilon(i) = 1 - \frac{u_a^+(i)}{u_r^+(i)} \qquad \dots (29)$$

where u_a^+ is the predicted value and u_r^+ is the corresponding reference value at a given $y^+(i)$ in a discretised velocity profile of N points. Figure 5 shows the variation of the diagnostic function with boundary layer height in inner scaling units y^+, with u_a^+ from Equation (6) and Equation
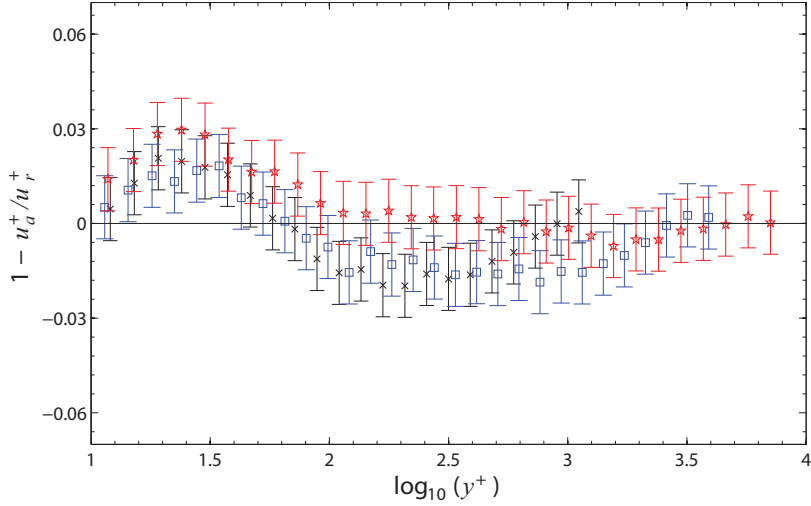
Figure 5. Percentage difference between the analytical and experimental mean velocity profiles in the wall-normal direction. Inner layer from Musker[30]. Symbols as in Table 1.

(5) from Musker[30]. The corresponding reference values $u_r^+(i)$ in Equation (29) are the three hot-wire traverses from Österlund[20] listed in Table 1.

The error function from each traverse is plotted using the same symbols as in Table 1. The uncertainty in the computed values of the diagnostic function due to the uncertainty in the hot-wire measurements from Table 2 is shown by error bars in Fig. 5. This allows assessing the inaccuracy of the analytical fit in the context of the experimental uncertainty. At $Re_\theta = 3,654$, 12,633 and 22,845, the diagnostic functions in Fig. 5 show an appreciable intercept with the $\varepsilon = 0$ line, with the intercept range being better at increasing Reynolds numbers. At $Re_\theta = 22,845$, shown by the ($\star$), the error bars intercept the $\varepsilon = 0$ line over the range $10^2 \leq y^+ \leq 10^4$, indicating a good agreement between the analytical model and the experimental velocity profile. The analytical profile appears less accurate in the region of transition between the viscous sub-layer and the logarithmic overlap region, with values of the diagnostic function further away from the $\varepsilon = 0$ line over the range $10 \leq y^+ \leq 30$.

Figure 6 shows the diagnostic function from the same three hot-wire traverses as Fig. 5, with u_a^+ in Equation 29 estimated from Equation 6 and Equation 4 from Spalding[29]. At $Re_\theta = 3,654$, 12,633 and 22,845, the diagnostic function shows a reasonable intercept with the $\varepsilon = 0$ line. The accuracy of the prediction in the transition region between the viscous sub-layer and the logarithmic overlap region is worse than in Fig. 5, with the percentage difference symbols further away from the $\varepsilon = 0$ line. This quantitative assessment using a diagnostic function seems to indicate that the compound velocity profile that uses an inner velocity profile derived from Musker[30] offers some predictive advantages over the range of Reynolds numbers tested.

4.3 Numerical and experimental velocity profiles

Figure 7 compares velocity profiles obtained by the interactive boundary layer model of Section 3.2 against the same benchmark data of Table 1, used in Fig. 2. In this application of the interactive boundary layer model, $n = 4$ was used for the numerical prediction of the mixing length in Equation 13. The symbols shown in Fig. 7 are the benchmark data[20-24] at the
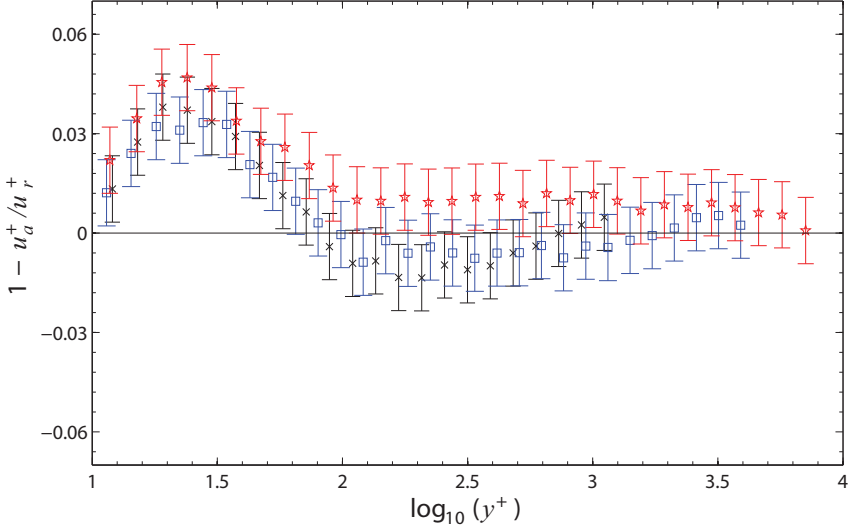
Figure 6. Percentage difference between the analytical and experimental mean velocity profiles in the wall-normal direction. Inner layer from Spalding[29]. Symbols as in Table 1.
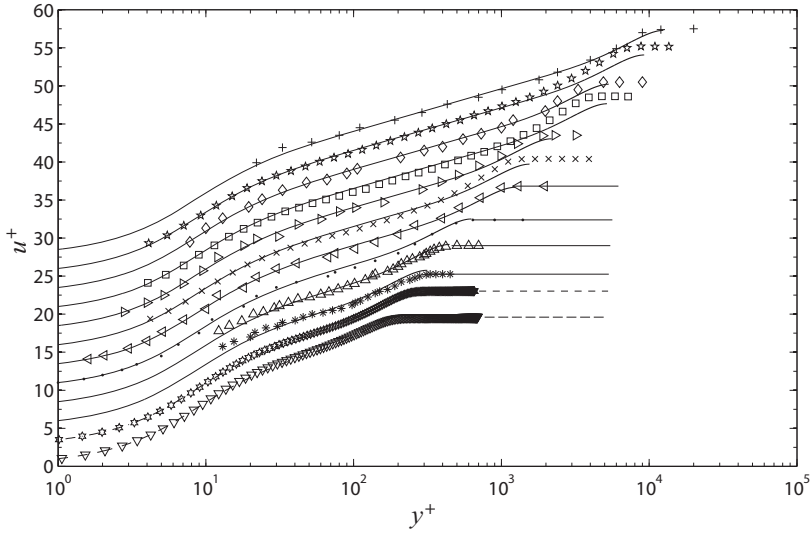

Figure 7. Turbulent boundary layer velocity profiles predicted by the interactive boundary layer model ($n = 4$). Symbols as in Table 1.

different Re_θ stated in Section 2, which have been labelled as in Table 1. The lines show the normalised numerical velocity profiles in wall units. For clarity, the same incremental shift of $u^+ = 2·5$ as in Fig. 2 is applied to all curves. The origin of the ordinate of Fig. 7 refers to the Re_θ = 422 profile. Figure 7 shows that the interactive boundary layer model of Section 3.2 produces a full velocity profile down to the wall. In the outer layer, the interactive boundary layer model captures the Reynolds number dependent transition between the logarithmic overlap region and the constant free-stream velocity for many of the curves. The free-stream velocity at Re_θ = 22,845, 12,663 and 3,654 appears to be under-predicted.
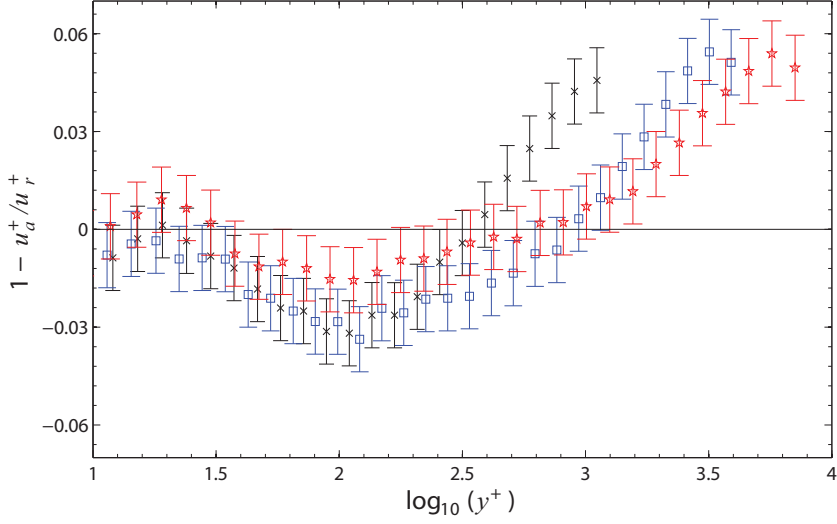
Figure 8. Percentage difference between the numerical and experimental mean velocity profiles in the wall-normal direction. Symbols as in Table 1.

A further insight into the accuracy of the predicted velocity profile prediction using the interactive boundary layer model is given in Fig. 8. In Fig. 8, the diagnostic function of Equation (29) is shown for the profiles at $Re_\theta = 22,845$, $12,663$ and $3,654$. These are the same three benchmark velocity profiles from Österlund[20] from Table 1 used in the assessment of the analytical velocity profile predictions in Figs 5 and 6. In evaluating Equation (29), u_a^+ is the normalised velocity predicted by the interactive boundary layer model at the same y^+ as the hot-wire wall-normal distance in the experiment. The error bars display the measurement uncertainty reported by Österlund[20]. The interactive boundary layer model confirms an appreciable predictive performance from the wall through the viscous sub-layer and the transition region up to the logarithmic overlap region. Over the range $30 \leq y^+ \leq 500$, the mean velocity appears to be somewhat over-predicted with respect to Figs 5 and 6.

The interactive boundary layer model does not directly prescribe a logarithmic trend on the predicted velocity profile but an approach to a logarithmic trend is obtained indirectly by the use of a mixing length model that is compatible with the log-law. This enforces self-similarity only parenthetically across the logarithmic region, this parenthetic similarity being driven by the persistence of Reynolds number scaling effects through the logarithmic region at small Re_τ. In a complementary expansion method, the logarithmic law represents an approximation of leading order in the small parameter Re_τ^{-1}, as discussed by Klewicki[39]. Therefore, the interactive boundary layer model, which uses the complementary expansion approach, is expected to exhibit a similar approximation in the logarithmic overlap region, which results in the over-prediction of the velocity displayed in Fig. 8 over the range $30 \leq y^+ \leq 500$. In the mixing layer, as $y^+ \rightarrow Re_\tau$, the predicted velocity profile remains below u_e^+, which is under-estimated by approximately 5%.

This difference between the normalised free-stream velocity from experiment and from the interactive boundary layer model is further investigated in Fig. 9, where the outer layer portion of the predicted velocity profile at $Re_\theta = 22,845$ is re-plotted on a larger scale. The continuous
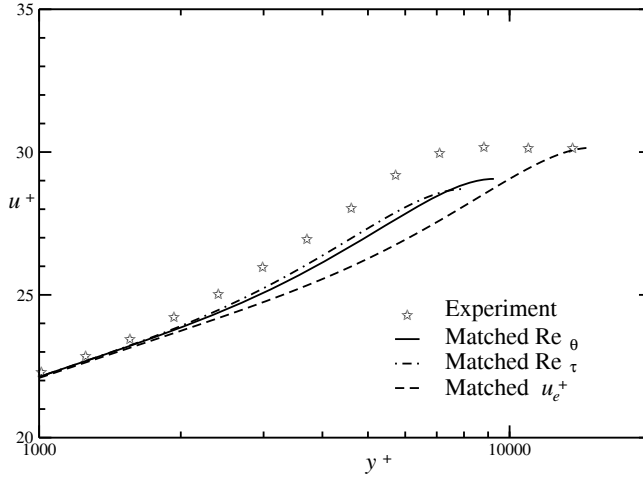
Figure 9. Outer layer profile plotted by the interactive boundary layer method. Re_θ = 22,845.
($\star$) experiment, (–), (– –), (– · –) interactive boundary layer model.

line is the numerical prediction obtained by matching the experimental value of Re_θ in the interactive boundary layer model, the dash-dot line is obtained by matching the experimental value of Re_τ, and the dashed line shows the predicted profile with a matched normalised free-stream velocity u_e^+. Matching the values of the experimental Reynolds number seems to give similar profiles irrespective of whether the target Reynolds number is defined with respect to the outer scaling variables $Re_\theta = u_e \theta/\nu$ or the inner scaling variables $u_\tau \delta/\nu$. Fitting the outer profile by imposing the normalised free-stream velocity u_e^+ seems to over-predict the boundary layer thickness, leading to a coarser agreement with experiment compared to the numerical predictions obtained by matching the profile Reynolds number.

This paper has not attempted to predict the time-averaged streamwise velocity profile of boundary layers at $Re_\tau = 422$ using the interactive boundary layer model. In this method, u_e^+ is obtained by matching the outer region velocity profile to the inner region velocity profile in the logarithmic overlap region. At $Re_\tau = 422$, an overlap region in the form of a logarithmic layer is no longer present, which prevents the method form evaluating u_e^+. Here the interactive boundary layer model in its present formulation has reached its lower Re_τ applicability limit.

4.4 The shear stress profile

Figure 10 compares the normalised mixing length distributions across a zero-pressure gradient boundary layer obtained by different numerical methods with the normalised $\ell(\eta)$ distribution obtained from measurements at Re_τ =1,540 by Klebanoff[40], reported in Hinze[41]. The normalised $\ell(\eta)$ distribution from Equation (12) is shown by the continuous line while the dashed line shows the distribution from Equation (13) with $n = 4$. It is also of interest to compare the present numerical predictions with older papers that devise mixing length distributions. For this purpose, the mixing length distributions from Spalding[18] and from Michel *et al*[17] are shown by dash and dot lines, based on the mean velocity profile provided by Galbraith and Head[19]. The dash-double-dot line shows the normalised $\ell(\eta)$ obtained from Spalding[18], as reported in
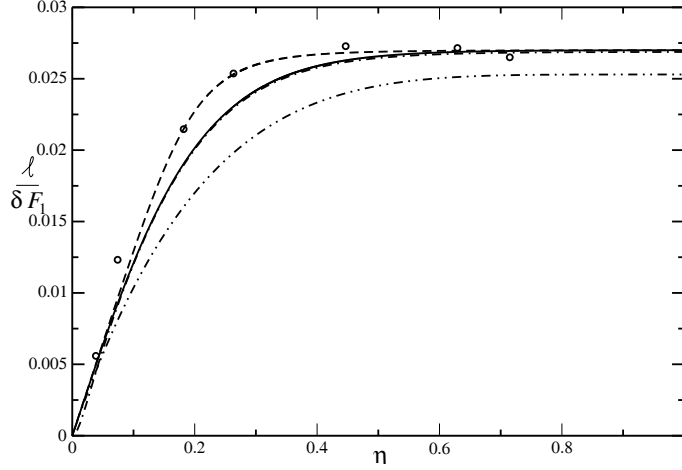
Figure 10. Normalised mixing length $\ell / (\delta F_1)$ versus normalised distance from the wall η.
($\circ$) experiment[40] at $Re_\tau = 1,540$, (-) interactive boundary layer model at $Re_\tau = 1,000$ with $F_1 = 3 \cdot 1479$ from Equation (12), (– –) interactive boundary layer model at $Re_\tau = 1,000$ with $F_1 = 3 \cdot 1044$ from Equation (13) ($n = 4$), (– · · –) mixing length model from Spalding[29] in Galbraith and Head[19] with $F_1 = 3 \cdot 1626$, (·) mixing length model from Michel et al[17] with the same Galbraith and Head[19] $F_1 = 3 \cdot 1626$ profile.

Galbraith and Head[19], and the dash-dot line overlapping the continuous line shows the corresponding result from Michel et al[17]. In this application of the mixing length model of Spalding[18], the normalised mixing length seems to be under-predicted with respect to the measurements, with the asymptotic value of the normalised mixing length for $\eta \to 1$ being up to 7% below the experimental trend line. This under-estimation can be partially explained by the uncertainty in the value of δ used in the normalisation, which is defined differently by different authors at between $0 \cdot 95 u_e$ and $0 \cdot 995 u_e$. The different values of F_1 in the normalisation play an important role in the observed discrepancy.

At $Re_\theta = 1,540$, the interactive boundary layer model gives a better estimate of the normalised mixing length distribution from experiment, compared to the Spalding[18] mixing length model, as shown by the proximity of the continuous line and of the dashed line to the circles in Fig. 10. The predictions are rather good when the interactive boundary layer model is used in conjunction with the new mixing length blending function of Equation (13), as shown by the dashed line (– –) in Fig. 10. As such, the new blending function appears to be a good improvement over the blending function of Equation (12). No effort has been made to further optimise $n \in \Re$ in Equation (13) by adding decimal digits.

Figure 11 shows the profile of the normalised eddy viscosity $v_t/(u_\tau F_1 \delta)$ across the same zero pressure gradient boundary layer of Fig. 10, where $v_t = \tilde{F}^2 \ell | \partial u/\partial y |$. The symbols are from the same experimental data set[40] as in Fig. 10 (open circles) to which further measurements by Townsend[42] at $Re_\tau = 2,775$ have been added (open squares). The curves with symbols and lines, ($\square$–$\square$) and ($\circ$–$\circ$), show two normalised eddy viscosity profiles from the direct numerical simulation (DNS) of Skote[21], obtained at $Re_\theta = 422$ and $Re_\theta = 588$. The continuous line and the dash-dot line show the predicted normalised eddy viscosity from the mixing length models of Spalding[18] and of Michel et al[17], based on a velocity profile provided by Galbraith and
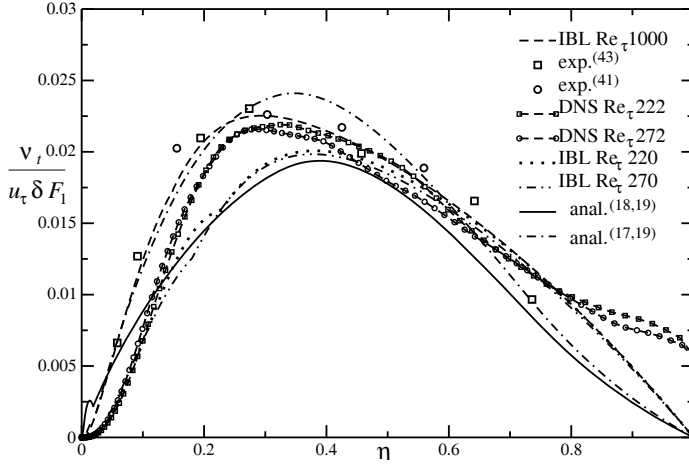
Figure 11. Normalised eddy viscosity $v_t / (u_\tau \delta F_1)$ versus normalised distance from the wall η (°). experiment [40] at $Re_\tau = 1,540$, (□) experiment [42] at $Re_\tau = 2,775$, (⋯) interactive boundary layer prediction at $Re_\tau = 220$ from Equation (13), (– –) interactive boundary layer prediction at $Re_\tau = 1,000$ from Equation (13) ($n = 4$), DNS from Skote [21] at (□ – – □) $Re_\tau = 222$ and at (° – – °) $Re_\tau = 272$. (–) Spalding [18] and (– · –) Michel et al [17] $\ell(\eta)$ models at $Re_\tau = 1,578$.

Head[19]. In this application, the Spalding[18] mixing length model under-predicts the eddy viscosity maximum from the measurement at $Re_\tau = 1,540$ by Klebanoff[40], as shown by the continuous line in Fig. 11. This under-prediction can be corrected by using the mixing length model of Michel et al[17] when tested as in Galbraith and Head[19], as shown in Fig. 11 by the dash-dot line. The normalised eddy viscosity distribution from the Michel et al[17] mixing length model remains not completely satisfactory, as the predicted normalised eddy viscosity maximum is higher than in experiment and occurs at $\eta = 0.35$, which is above the wall-normal distance at which v_t is maximum both in experiment and in the direct numerical simulation of Skote[21]. Across the mixing region of the boundary layer, over the range $0.5 \leq \eta \leq 1$, all models predict a monotonic decay in the normalised v_t fitting the boundary condition $v_t = 0$ at $\eta = 1$. This is consistent with the normalised experimental v_t distributions reported in Galbraith and Head[19], Fig. 11(a), that indicate the trend $v_t \to 0$ as $\eta \to 1$.

Figure 11 shows by the dotted line the normalised eddy viscosity profile obtained at $Re_\tau = 220$ using the interactive boundary layer model of Cousteix and Mauss[15,16] with the mixing length model of Michel et al[17] and Equation (13) as the mixing length blending function. At $Re_\tau = 220$, the model under-predicts the normalised eddy viscosity maximum and the predicted profile displays a discontinuous gradient at $\eta = 0.24$. A similar discontinuity is predicted at $Re_\tau = 270$ by the same model at $\eta = 0.20$. This discontinuity is associated to the asymptotic matching in the numerical method, which matches the value of the mean velocity and that of the velocity gradient between the inner and outer layer solutions at a common location in the overlap region, but not the velocity profile curvature. This results in the discontinuity in slope shown in Fig. 11.

At the higher Reynolds number of $Re_\tau = 1,000$, using the interactive boundary layer model of Cousteix and Mauss[15,16] with the new mixing length blending function of Equation (13) gives appreciably improved predictions, as shown by the dashed curve in Fig. 11. The normalised eddy viscosity maximum is captured well both in magnitude and in position along η, to about the same extent as with the Michel et al[17] model, shown by the dash-dot line in Fig. 11.

Over the range $0.5 \leq \eta \leq 1$ the normalised ν_t distribution predicted by using the new mixing length blending function of Equation (13) gives an improved match to the benchmark data, compared to the predictions from the Spalding[18] mixing length model in Galbraith and Head[19]. Over this range, ν_t is predicted to be monotonically decreasing with a monotonically convex trend, which appears to better follow the experimental and the DNS benchmark data. From a physical viewpoint, it is questionable whether the boundary condition $\nu_t = 0$ at $\eta = 1$ displayed by all the models is appropriate, given that the DNS displays a finite and positive value of ν_t at $\eta = 1$. As discussed in Rona and Grottadaurea[11], the definition of the boundary layer thickness δ is rather arbitrary and is linked to the engineering practice of deeming wall-driven viscous effects not significant at $y > \delta$. A vanishingly small mean velocity gradient exists outside the boundary layer, which can be used for representing the Reynolds stress effects due to the free-stream turbulence on the mean flow by the Boussinesq approximation, using a finite value of ν_t. The flat plate boundary layer experiments listed in Table 1 were obtained under controlled conditions in wind tunnels designed for low free-stream turbulence. At these conditions, the effects of free-stream turbulence on the boundary layer mean velocity profile are small. Therefore, zero as well as finite values of ν_t at $\eta = 1$ appear to be appropriate choices for modelling this class of flows. The zero value of ν_t appears to be appropriate for modelling flows for which the free-stream turbulence intensity level is not known *a priori*. As a numerical experiment, the target Reynolds number in the interactive boundary layer model was varied over the range $1{,}000 \leq \mathrm{Re}_\tau \leq 2{,}775$ and was found to have very little effect on the predicted normalised ν_t, which is also the trend in experiment[40,42].

5.0 ADVERSE PRESSURE GRADIENT BOUNDARY LAYER

5.1 Analytical predictions

The methods presented in Section 3 are now tested against direct numerical simulation data in order to assess the accuracy of the methods in predicting a non-zero pressure gradient turbulent boundary layer mean velocity profile. The pressure gradient is expressed through the Clauser parameter

$$\beta_c = \frac{\delta}{u_\tau} \frac{dp}{dx} \qquad \qquad \dots (30)$$

The main flow parameters characterising the adverse pressure gradient boundary layer test cases are summarised in Tables 1 and 4. The values in Table 4 are the ones reported in the numerical work of Skote[21] for boundary layers developing under a low adverse pressure gradient (APG1, $\beta_c = 0.24$) and a moderate adverse pressure gradient (APG2, $\beta_c = 0.65$), respectively. Π has been evaluated from Equation (7) using the values of u_e, u_τ, and δ from Skote[21], reported in Table 1, and $\kappa = 0.384$ and $B = 4.17$ from Monkewitz *et al*[33]. The aim of this work is to predict analytically the normalised streamwise velocity distribution across a turbulent boundary layer growing under a mild to moderate adverse pressure gradient that can be used as an inflow condition in computational fluid dynamics. In such application, the target boundary layer velocity distribution is typically unknown *a priori* and only target values for u_e, u_τ and δ are known, obtained, for

Table 4
DNS velocity profiles at low (APG1) and moderate (APG2) adverse pressure gradients. Right-hand side of the table: $n = 24$ in Equation (13).

DNS	β_c	Re_θ	Π	$(Re_\tau)_n$	$(u_e^+)_n$
APG1	0·24	606	0·38	250	21
APG2	0·65	681	0·45	250	22·3
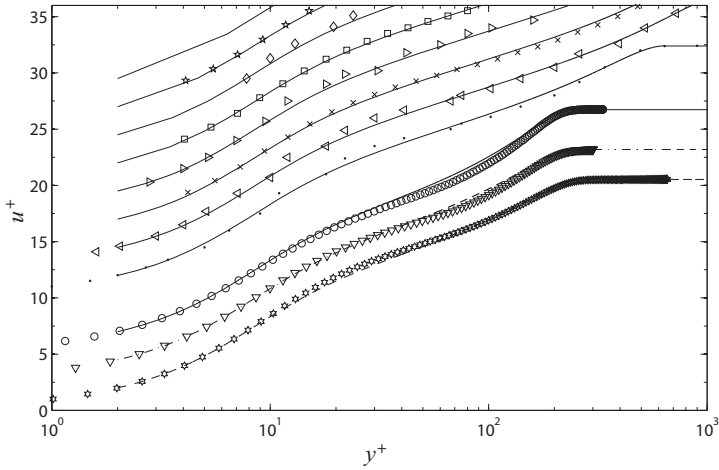
Figure 12. Adverse pressure gradient turbulent boundary layer velocity profiles fitted to Equation (6). Symbols as in Table 1.

instance, by correlation-type design methods. The present work tests the analytical method in such an *a priori* application. For cases where more complete velocity profile data are available, for instance, from experiment, Rona and Grottadaurea[11] show that improved estimates of Π, κ, and B can be obtained by fitting Equation (6) using the least squares fit method.

Figure 12 shows by the symbols of Table 1 the reference velocity profiles from Section 2 and by the lines the corresponding analytical predictions from Equations (5) and (6). The first three mean velocity profiles at the bottom Fig. 12, plotted with symbols ($\vartheta,\nabla,\circ$) are from direct numerical simulations with zero, low, and moderate adverse streamwise pressure gradients respectively. The corresponding analytical mean velocity profiles for the zero pressure gradient (dashed line), low adverse pressure gradient (dashed line), the moderate adverse pressure gradient (continuous line) are shown overlaid on the direct numerical simulation data. For clarity, a vertical shift of $u^+ = 2\cdot5$ has been applied to the adverse pressure gradient profiles and the origin of the vertical axis in Fig. 12 refers to the $Re_\theta = 588$ mean velocity profile. The zero pressure gradient profiles from experiment at higher Reynolds numbers are reproduced from Fig. 2 in Fig. 12 to allow a comparative assessment of the quality of the analytical predictions across the Reynolds number range $422 \leq Re_\theta \leq 31,000$, with and without pressure gradient. The experimental velocity profile for $Re_\theta = 1,430$, designated by ($\cdot$), is vertically offset by $u^+ = 10$ from the origin. An incremental shift of $u^+ = 2\cdot5$ has been applied to the remaining profiles. The composite law of the wall of Equation (6), with the inner layer velocity distribution predicted by Equation (5) from Musker[30], captures most of the u^+ dependence on β_c, δ, u_e, u_τ and Re_θ. The
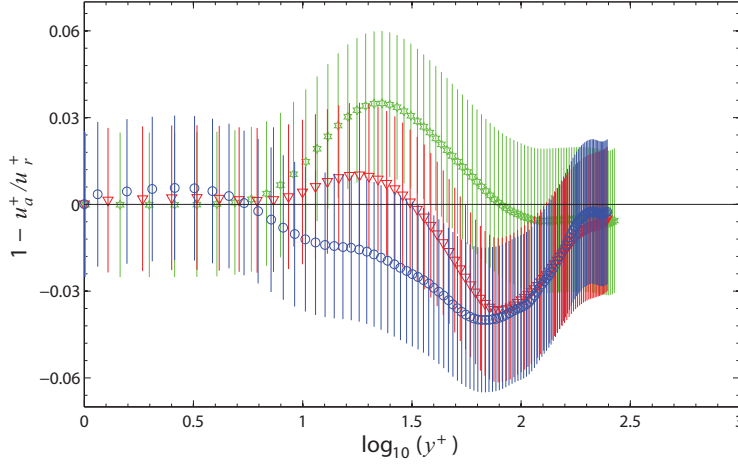
Figure 13. Percentage difference between the analytical and numerical velocity data in the wall-normal direction. Symbols as in Table 1.

quality of the predictions from this analytical method appears to be consistent across the Reynolds number range $422 \leq \mathrm{Re}_\theta \leq 31{,}000$.

Figure 13 gives a further quantitative insight into the predictive performance of the composite law of the wall of Equations (5) and (6) in the presence of an adverse pressure gradient at low Re_θ. The diagnostic function of Equation (29) is used to evaluate the percentage difference between three mean velocity profiles from the direct numerical simulations of Skote[21] and the predicted velocity profiles. In this application of the diagnostic function, u_r^+ is the benchmark velocity value from the direct numerical simulation at the non-dimensional wall-normal distance y^+ from the modelled wall. u_a^+ is the corresponding non-dimensional velocity predicted by the analytical method at the same y^+ through the boundary layer.

The error bars display the uncertainty in u_r^+ due to the mesh convergence of the direct numerical simulations, which was evaluated from the APG1 mesh independence study of Skote *et al*[22]. The same uncertainty is assumed for the ZPG u350 and APG2 direct numerical simulation predictions. As the three numerical simulations are conducted at similar Reynolds numbers, covering the narrow range $251 \leq \mathrm{Re}_\tau \leq 272$, the differences in the trends displayed in Fig. 13 reflect primarily the variation in the non-dimensional streamwise pressure gradient β_c among the test cases, rather than of δ and u_τ. The diagnostic function for the zero pressure gradient test case, shown by (✿), shows an appreciable agreement between the predicted and the reference velocity profiles across the boundary layer, with some variance in the blending region between the viscous sub-layer and the logarithmic overlap region, where the analytical profile under-predicts the normalised mean streamwise velocity. With the mild adverse pressure gradient of APG1, the variance in the blending region is reduced but an over-prediction of the normalised mean streamwise velocity appears in the logarithmic overlap region. This over-prediction accentuates with increasing β_c in APG2, which is the moderate adverse pressure gradient case. In all three cases, the differences between the prediction and the benchmark data are of the same order of magnitude as the estimated uncertainty in the benchmark data.

This confirms that the numerical method retains an appreciable predictive ability at low and moderate adverse streamwise pressure gradients in the context of the uncertainty associated with the benchmark data.
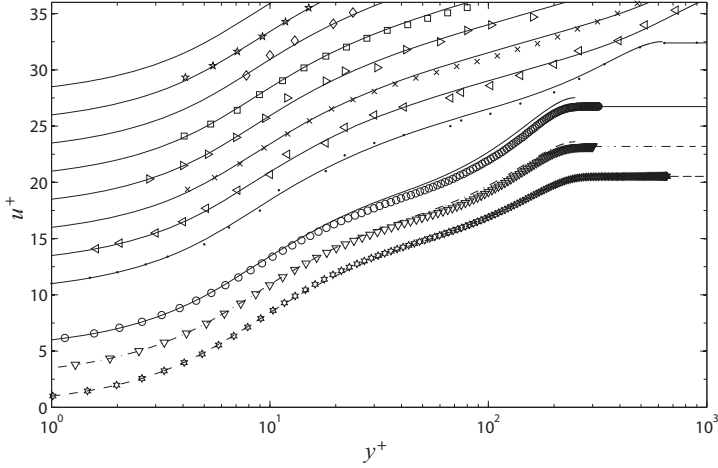
Figure 14. Zero and adverse pressure gradient boundary layer velocity profiles predicted by the interactive boundary layer model ($n = 4$). Symbols as in Table 1.

5.2 Interactive boundary layer model predictions

Figure 14 shows the predicted streamwise velocity profiles in presence of a low and a moderate adverse streamwise pressure gradient, obtained from the interactive boundary layer model. These are compared against the direct numerical simulation mean velocity profiles from Skote[21] at $Re_\theta = 606$ and $Re_\theta = 681$, listed in Table 1. These are the same benchmark profiles used in Section 5.1 for which the adverse pressure gradient is expressed as the Clauser parameter, as stated in Table 4.

For the interactive boundary layer model, two values of the constant n in Equation (13) in the mixing length model are tested. These are $n = 4$ and $n = 24$. The profiles in Fig. 14 are obtained with $n = 4$. The predictions from the interactive boundary layer model show that this numerical method generates the correct qualitative response to the change in streamwise pressure gradient, which is a progressive increase of the streamwise velocity above a constant logarithmic gradient in the mixing region, over the range $0{\cdot}2\,Re_\tau \leq y^+ \leq Re_\tau$. This increment is somewhat over-estimated by the interactive boundary layer model, resulting in some over-estimation of u_e^+ that is more pronounced at $Re_\theta = 681$, which is the highest adverse pressure gradient tested. This is highlighted in Fig. 14 by a small vertical gap between the interactive boundary layer model profile at $y^+ = 250$ (solid line through the circles) and the $u^+ = u_e^+$ horizontal line to the right of it. This vertical gap is smaller in the interactive boundary layer model predictions at the lower adverse pressure gradient of $\beta_c = 0.24$, shown by the dash-dotted line, and essentially vanishes in the zero streamwise pressure gradient predictions shown by the dashed line. This trend is confirmed by the diagnostic function reported in Fig. 15, which indicates a progressive decrement in $1 - u_a^+/u_r^+$ with increasing values of β_c, away from the target $1 - u_a^+/u_r^+ = 0$ line. In this application of the diagnostic function, u_a is the velocity prediction from the interactive boundary layer method and u_r is the corresponding benchmark velocity value from Skote[21]. As in Fig. 13, the error bars in Fig. 15 show the uncertainty estimate of the reference data u_r, so that the discrepancy between the velocity profiles from the interactive boundary layer model and the reference profiles can be discussed in the context of the
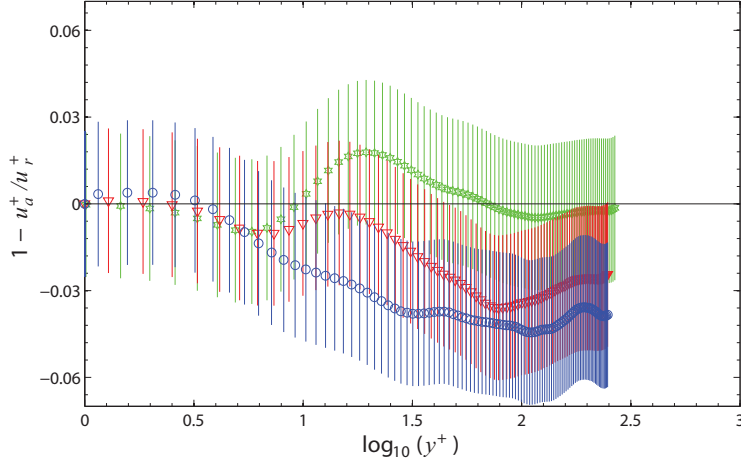
Figure 15. Percentage difference between the benchmark and the numerical velocity data in the wall-normal direction with and without adverse pressure gradient. $n = 4$ in Equation (13). Symbols as in Table 1.

uncertainty of the reference data. With a zero pressure gradient, the interactive boundary layer predictions lie within the uncertainty band of the reference data, as shown by the $1 - u_a^+/u_r^+ = 0$ line intercepting the error bars from the $Re_\theta = 588$ profile (✿) across the whole boundary layer. With increasing adverse pressure gradient, this intercept is limited to progressively lower values of y^+, showing a velocity over-prediction by the interactive boundary layer model beyond the statistical uncertainty of the reference data. As the interactive boundary layer model embeds a parallel flow assumption in its formulation, its predictions progressively deteriorate as the flow becomes more divergent under the influence of the adverse streamwise pressure gradient.

Figure 16 shows the sensitivity of the interactive boundary layer predictions on the exponent of the new mixing length blending function of Equation (13). This is done by computing the value of the diagnostic function defined as for Fig. 15, in which u_a is obtained from the interactive boundary layer model with $n = 4$ (open symbols) and $n = 24$ (filled symbols). The curves with the open symbols are identical to those of Equation (15) and the error bars associated to these curves are omitted for clarity. Increasing n from 4 to 24 in Equation (13) gives a sharper transition between the asymptotic values of ℓ in the inner and outer regions. This results in an improvement in the predicted mean velocity profile under a mild adverse pressure gradient, with a lower discrepancy between the predicted and reference velocity in the outer layer. Specifically, Fig. 16 shows that, at $Re_\theta = 606$ and $\beta_c = 0\cdot24$, the diagnostic function from the interactive boundary layer model with $n = 24$, shown by the filled triangles, is above the one from using $n = 4$, shown by the open triangles, and is closer to the $1 - u_a^+/u_r^+ = 0$ line. The error bars about the filled triangles represent the estimated uncertainty band of the benchmark data u_r. There is an appreciable intercept between this band and the $1 - u_a^+/u_r^+ = 0$ line across a significant portion of the boundary layer thickness. This shows that increasing the value of n to 24 in the blending function used in the interactive boundary layer model generates streamwise velocity predictions that fall within the uncertainty band of the benchmark values for a significant portion of the velocity profile.
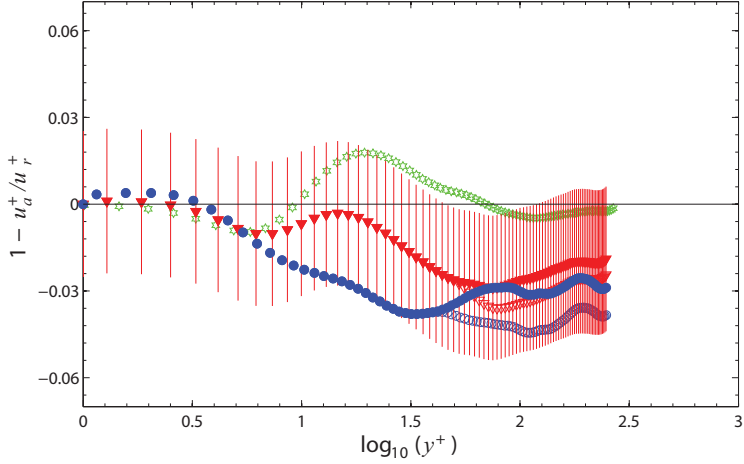
Figure 16. Percentage difference between the benchmark and the numerical velocity data in the wall-normal direction with and without adverse pressure gradient. Open symbols *n* = 4, filled symbols *n* = 24. Symbols as in Table 1.

At $\text{Re}_\theta = 681$, under the adverse pressure gradient of $\beta_c = 0.65$, the boundary layer predicted by the interactive boundary layer model with $n = 24$ improves over the one predicted with $n = 4$. This is shown by the respective diagnostic functions in Fig. 16, in which the $n = 24$ diagnostic function, shown by the filled circles, becomes closer to the $1 - u_a^+/u_r^+ = 0$ line than the $n = 4$ diagnostic function, shown by the open circles. This improvement however falls short of placing this profile within the $\pm 2.5\%$ uncertainty band of the benchmark data across the outer layer. Further analysis on the non-dimensional shear stress and the non-dimensional turbulent viscosity shows that increasing n improves the agreement between the DNS results and the mean velocity profile from the interactive boundary layer model. A slope mismatch remains between the interactive boundary layer streamwise velocity predictions and the velocity profile from the direct numerical simulation, regardless of the value of n. To this extent, an improved multi-parameter mixing length model could be designed to better fit the non-dimensional turbulent shear stress distribution across the turbulent boundary layer.

5.3 Limitations of the numerical methods

The limitations of the numerical methods used in this paper can be determined from two different perspectives. The first perspective stems from the analysis of the formal assumptions in the formulation of the numerical scheme. The second more heuristic approach stems from the comparison of the predictive performance of the scheme against alternative methods and benchmark data. Following the first approach, the interactive boundary layer model is restricted to zero pressure gradient boundary layers from its parallel flow assumption. It is further restricted to $\text{Re}_\theta \geq 300$ by the requirement of matching the inner and outer mean velocity profiles in the overlap region, which implicitly implies a logarithmic overlap by the choice of the mixing length model. The eddy viscosity model also assumes a fully developed turbulent flow.

Notwithstanding these formal restrictions, the interactive boundary layer model is shown in practice to have a wider applicability in Section 5.2, subject to the ability of accepting a

margin of error in the predictions. The approach of extending the applicability of a numerical scheme based on the acceptance of a degree of approximation in the predictions is similar to the extension of Reynolds averaged Navier-Stokes (RANS) schemes to time-dependent Reynolds averaged Navier-Stokes computations in Rona[43], in which the Wilcox $k - \omega$ two-equation RANS turbulence closure model is used in time-dependent flow predictions. In this work, the interactive boundary layer model is shown to retain an engineering accurate predictive ability for a boundary layer under a mild adverse streamwise pressure gradient, with the predictions degrading as the adverse pressure gradient becomes greater in magnitude.

This work used direct numerical simulation predictions from Skote[21] as benchmark for the interactive boundary layer model. The mean velocity profiles are compared at the same Reynolds number. Evaluating the non-dimensional parameter Re_τ from the DNS data is non-trivial. Re_τ is defined as the normalised wall-normal distance y^+ at which either (1) the normalised velocity profile gradient du^+/dy^+ is zero, (2) the turbulent shear stress τ^+ from Equation (17) is zero, or (3) the normalised eddy viscosity is zero.

The first two conditions provide the same value of Re_τ. The non-dimensional turbulent viscosity is given by

$$\frac{\tau^+}{\dfrac{du^+}{dy^+}} = Re_\tau \frac{\nu_t}{u_\tau \delta} = \frac{\nu_t}{\nu} = \nu^+ \qquad \ldots (31)$$

It is numerically equivalent to the edge of the boundary layer when $\tau^+ \to 0$ and $du^+/dy^+ \to 0$.

Figure 17 shows the function $\tau^+ / \dfrac{du^+}{dy^+}$ obtained from the DNS computations of Skote[21]. A

hump in the region $y^+ \in [250,300]$ leads to an overestimation of Re_τ with respect to the definitions 1 and 2. It is worth to note that the DNS computational domain is approximately as large as the maximum value of y^+ in Fig. 17, therefore the hump could be the result of a boundary effect of the numerical domain.

6.0 CONCLUSIONS

Numerical and analytical methods for obtaining the time-mean velocity profiles of a turbulent boundary layer are presented and validated against experimental data and direct numerical simulations.

Composite laws of the wall using profiles from Spalding[29] and Musker[30] in the inner layer and the law of the wake by Finley *et al*[12] in the outer layer give an analytical prediction across the full boundary layer that matches both the free stream velocity and the velocity gradient at the boundary layer edge.

By the use of a diagnostic function, the profiles were shown to give predictions within the estimated uncertainty band of the reference benchmark data across most of the boundary layer thickness. The explicit form of the Musker[30] profile in Monkewitz *et al*[33] gives an explicit composite law of the wall that is more practical to include in a computational fluid dynamic code and that generates engineering accurate streamwise velocity profiles over the Reynolds number range $422 \leq Re_\theta \leq 31{,}000$.

The authors propose a modification to the interactive boundary layer model of Cousteix and Mauss[15] with a new blending function for the mixing length in the outer region. Comparison against experimental data shows that the new blending function improves the prediction of the
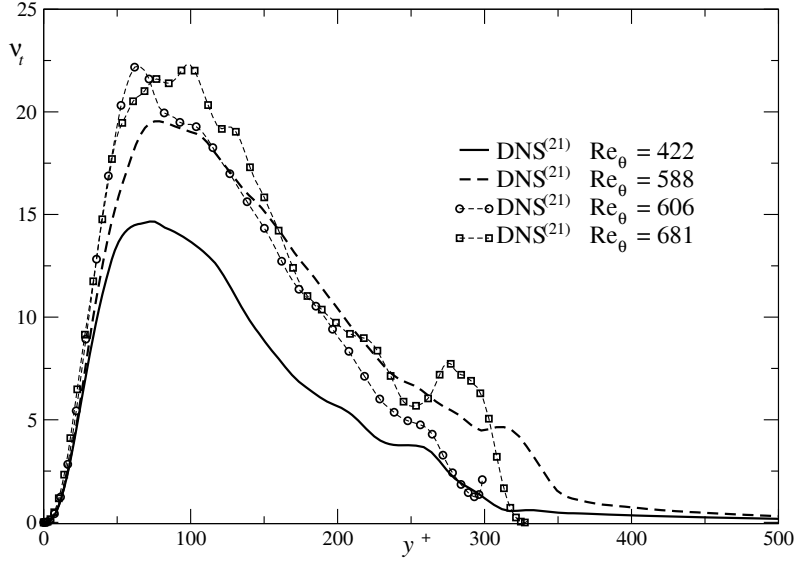
Figure 17. DNS analysis, v^+ versus y^+.

mixing length and of the eddy viscosity in outer region of a zero pressure gradient boundary layer, compared to the blending function of Michel *et al*[17] and the Spalding[18] mixing length model in Galbraith and Head[19]. The new method is validated against experimental and direct numerical simulation velocity profile data over the Reynolds number range $422 \leq \mathrm{Re}_\theta \leq 31,000$ under zero streamwise pressure gradient and found to achieve engineering accurate predictions in the inner layer and in the overlap region. The interactive boundary layer model in its present form is able to match a target Re_τ or a target free-stream velocity u_e^+. When a close match to both values is required by a specific engineering application, the composite law of the wall approach is more appropriate. The new blending function in the interactive boundary layer model introduces an additional adjustable parameter $n \in \Re$ that can undergo a more extensive calibration over a wider experimental data-set to further improve the predictions.

The comparison between the predictions from the analytical method and direct numerical simulations in the presence of an adverse pressure gradient shows an engineering accurate match of the mean velocity profiles. The diagnostic function analysis of these profiles indicates that the predicted profile under a mild adverse pressure gradient is mostly within the estimated uncertainty band of the reference benchmark data. This shows that the analytical method can be used for predicting adverse pressure gradient boundary layer flows over the Clauser parameter range $0 \leq \beta_c \leq 0.65$, at low Reynolds numbers. With the interactive boundary layer model, the difference between the predicted and the benchmark data can be reasonably matched to that of the analytical predictions by adjusting n from $n = 4$ to $n = 24$. The proposed blending function in the mixing length model improves the agreement with the direct numerical simulations, showing the practical value of this formulation. It is shown that, by varying n, the discrepancy between the predicted and the reference free-stream velocity can be reduced but cannot be eliminated. This gives scope for further improvements in the interactive boundary layer model, for instance, by the addition of a multi-parameter mixing length model, in future work.

ACKNOWLEDGMENTS

REFERENCES

1. ROWLEY, C., COLONIUS, T. and BASU, A. On self-sustained oscillations in two-dimensional compressible flow over rectangular cavities, *J Fluid Mech,* 2002, **455**, pp 315-346.
2. MILLIKAN, C.B. A critical discussion of turbulent flows in channels and circular tubes, 1938, Wiley (Ed.), Fifth International Congress on Applied Mechanics, New York, pp 386-392.
3. VON KÁRMÁN, T. Mechanische Aehnlichkeit und Turbulenz, 1930, Third international congress on applied mechanics, Stockholm, Sweden, pp 85-93.
4. COLES, D. The law of the wake in the turbulent boundary layer, *J Fluid Mech,* 1956, **1**, pp 191-226.
5. CHAUHAN, K. MONKEWITZ, P. and NAGIB, H. Criteria for assessing experiments in zero pressure gradient boundary layers, *Fluid Dynamics Research*, 2009, **41**, (2), pp 1-23, article number 021404.
6. PANTON, R. Review of wall turbulence described by composite expansions, *Applied Mech Reviews*, 2005, **58**, (1), pp 1-36.
7. BUSCHMANN, M. and GAD-EL-HAK, M. Recent developments in scaling of wall-bounded flows, *Prog in Aerospace Sci*, 2007, **47**, pp 419-467.
8. LEWKOWICZ, A. An improved universal wake function for turbulent boundary layers and some of its consequences, FLUGWISS, Z., *Weltraumforsch*, 1982, **6**, pp 261-266.
9. SANDHAM, N. An alternative formulation of the outer law of the turbulent boundary layer, 1991, Technical report DLR IB 221-91 A 10, DLR, Göttingen.
10. ÖRLÜ, R., FRANSSON, J. and ALFREDSSON, P. On near wall measurements of wall bounded flows - The necessity of an accurate determination of the wall position, *Prog in Aerospace Sci*, 2010, **46**, pp 353-387.
11. RONA, A. and GROTTADAUREA, M. Generalized Cole's law and outer layer conformal mapping, *J Hydraulic Research*, 2010, **48**, (5), pp 674-679.
12. FINLEY, P., POE, K. and POH, C. Velocity measurements in a thin turbulent water layer, *La Houille Blanche*, 1966, **21**, (6), pp 713-721.
13. ZAGAROLA, M.V. and SMITS, A.J. Mean-flow scaling of turbulent pipe flow, *J Fluid Mech*, 1998, **373**, pp 33-79.
14. WILCOX, D. *Turbulence Modeling for CFD*, Second Edition, 2002, D.C.W. Industries.
15. COUSTEIX, J. and MAUSS, J. *Asymptotic Analysis and Boundary Layers*, 2007, Springer-Verlag, Berlin Heidelberg.
16. COUSTEIX, J. and MAUSS, J. Interactive boundary layers in turbulent flow, *C.R. Mecanique*, 2007, **335**, pp 590-690.
17. MICHEL, R., QUEMARD, C. and DURANT, R. Application d'un schéma de longueur de mélange à l'étude des couches limites turbulentes d'équilibre, 1969, Technical Note, 154, ONERA.
18. SPALDING, D. The distribution of mixing length in turbulent flows near walls, 1965, Report TWF/TN/1, Imperial College.
19. GALBRAITH, R. and HEAD, M. Eddy viscosity and mixing length from measured boundary layer developments, *Aero Quarterly*, 1975, **26**, pp 133-154.
20. ÖSTERLUND, J.M. Experimental Studies of Zero Pressure-Gradient Turbulent Boundary Layer Flow, 1999, PhD thesis, Royal Inst Techn, KTM, Stockholm.
21. Skote, M. Studies of Turbulent Boundary Layer Flow Through Direct Numerical Simulation, PhD thesis, KTH, Sweden, 2001.
22. SKOTE, M., HENNINGSON, D. and HENKES, R. Direct numerical simulation of self-similar turbulent boundary layers in adverse pressure gradients, *Flow, Turbulence and Combustion*, 1998, **60**, pp 47-85.
23. ERM, L. and JOUBERT, P.N. Low-Reynolds-number turbulent boundary layers, *J Fluid Mech*, 1991, **230**, pp 1-44.

24. DE GRAAF, D. and EATON, J. Reynolds-number scaling of the flat-plate turbulent boundary layer, *J Fluid Mech*, 2000, **422**, pp 319-346.
25. RONA, A. and SOUEID, H. Boundary layer trips for low Reynolds number wind tunnel tests, 2010, Conference paper 2010-399, American Institute of Aeronautics and Astronautics, Orlando, FL, USA, 48th AIAA Aerospace Sciences Meeting including the New Horizons Forum and Aerospace Exposition, January 2010.
26. ROTTA, J. Das in wandnähe gültige Geschwindigkeitsgesetz turbulenter Strömungen, *Ing Arch*, 1950, **18**, pp 277-280.
27. REICHARDT, H. Vollständige Darstellung der Turbulenten Geschwindigkeitsverteilung in glatten Leitungen, *Angew, Z.*, *Math Mech*, 1951, **31**, pp 208-219.
28. VAN DRIEST, E. On turbulent flow near a wall, *J Aerospace Sci*, 1956, **23**, pp 1007-1011.
29. SPALDING, D. A single formula for the law of the wall, *Transactions of ASME J Applied Mechanics*, 1961, ASME **83**, p 445.
30. MUSKER, A. Explicit expression for the smooth wall velocity distribution in a turbulent boundary layer, *J American Institute of Aeronautics and Astronautics*, 1979, **17**, pp 655-657.
31. NITSCHE, W., THÜNKER, R. and HABERLAND, C. A computational Preston tube method, 1983, Fourth symposium on turbulent shear flows, Karlsruhe, West Germany, 12-14 September 1983, pp 261-276.
32. KENDALL, A. and KOOCHESFAHANI, M. A method for estimating wall friction in turbulent wall-bounded flows, *Experiments in Fluids*, 2008, **44**, pp 773-780.
33. MONKEWITZ, P. CHAUHAN, K. and NAGIB, H. Comparison of mean flow similarity laws in zero pressure gradient turbulent boundary layers, *Physics of Fluids*, **20**, (105102).
34. MOSES, H. The behavior of turbulent boundary layers in adverse pressure gradient, 1964, Technical Report 73, Gas Turbine Laboratory, MIT, Cambridge, MA, USA.
35. KROGSTAD, P., ANTONIA, R. and BROWNE, L. Comparison between rough- and smooth-wall turbulent boundary layers, *J Fluid Mech*, 1992, **245**, pp 599-617.
36. PRANDTL, L. Bericht über Untersuchungen zur ausgebildeten Turbulenz, *ANGEW, Z.*, *Math Mech,* 1925, **5**, 136-139.
37. VAN DRIEST, E.R. On dimensional analysis and the presentation of data in fluid-flow problems, *ASME J Applied Mathematics*, 1946, **13**, (1), pp 34-40.
38. COUSTEIX, J. Outer boundary layer self-similar solution, private communication (2009).
39. KLEWICKI, J. Reynolds number dependence, scaling, and dynamics of turbulent boundary layers, *ASME J Fluids Eng*, 2010, **132**, (94001), pp 1-48.
40. KLEBANOFF, P.S. Characteristics of turbulence in a boundary layer with zero pressure gradient, 1954, Technical Note 3178, National Advisory Committee for Aeronautics (NACA).
41. HINZE, J.O. *Turbulence*, 1975, McGraw-Hill, New York.
42. TOWNSEND, A.A. The structure of the turbulent boundary layer, *Mathematical Proceedings of the Cambridge Philosophical Society*, 1951, **47**, (2), pp 375-395.
43. RONA, A. Self-excited supersonic cavity flow instabilities as aerodynamic noise sources, *Int J of Aeroacoustics,* 2006, **5**, (4), pp 335-360.